Hot-spot generation and growth in shocked plastic-bonded explosives studied by optical pyrometry

Cite as: J. Appl. Phys. **125**, 215904 (2019); https://doi.org/10.1063/1.5098476
Submitted: 02 April 2019 . Accepted: 17 May 2019 . Published Online: 06 June 2019

Will P. Bassett, Belinda P. Johnson, Lawrence Salvati, and Dana D. Dlott

Journal of Applied Physics ARTICLE scitation.org/journal/jap

Hot-spot generation and growth in shocked plastic-bonded explosives studied by optical pyrometry

Cite as: J. Appl. Phys. **125**, 215904 (2019); doi: 10.1063/1.5098476
Submitted: 2 April 2019 · Accepted: 17 May 2019 ·
Published Online: 6 June 2019

Will P. Bassett,[a] Belinda P. Johnson, Lawrence Salvati III, and Dana D. Dlott[b]

AFFILIATIONS

School of Chemical Sciences and Fredrick Seitz Materials Research Laboratory, University of Illinois at Urbana-Champaign, Urbana, Illinois 61801, USA

[a]**Present address:** Lawrence Livermore National Laboratory, 7000 East Ave., Livermore, California 94550, USA.
[b]**Author to whom correspondence should be addressed:** dlott@illinois.edu

ABSTRACT

The aggregate behavior of hot spots in shocked plastic-bonded explosives (PBX) was studied by nanosecond optical pyrometry. The averaged thermal emission spectra from at least 25 tiny (50 μg) explosive charges of a pentaerythritol tetranitrate PBX, at several impact velocities from 1.5 to 4.5 km/s, was used to determine average temperatures and emissivities. Individual spectra were analyzed to determine the distribution of hot spot temperatures in individual charges with unique microstructures. Understanding shocks in tiny charges with different microstructures is needed to understand shocks in large PBX charges which sample many microstructures as they propagate. The initial hot spot density was several percent, and the average initial hot spot temperature of 4000 K was, surprisingly, independent of impact velocity. With underdriven shocks, the initial hot spot temperatures clustered around 4000 K, but with overdriven shocks, there were both hotter and colder hot spots. The initial hot spot density increased quadratically with impact velocity. The generation of hot spots was described by a model with a threshold energy to trigger hot spot formation and a distribution of energetic barriers to hot spot formation.

I. INTRODUCTION

Hot spots play a critical role in the shock to detonation transition of plastic-bonded explosives (PBX),[1–4] and understanding and controlling hot spots would permit the development of safer explosives less sensitive to accidental insults. A PBX is an aggregate of explosive crystals and polymer binder with a complex microstructure.[4,5] When a shock passes through a PBX, it encounters regions with different microstructures and different local concentrations of explosive and binder. Some of these regions can concentrate the shock energy, which can result in localized exothermic chemical reactions that create hot spots.[2,4] The existence and behavior of hot spots is largely inferred based on other observations,[6–8] or simulations,[9–17] since tiny transient hot spots are difficult to observe when the material is exploding. Many theoretical investigations of hot spots considered hot spot formation by the collapse of a single void.[18] The collapse of a void in a reactive medium has been studied with reactive burn models[3,19] or molecular dynamics with reactive classical potentials.[9,20–24] Tarver and co-workers[19] used reactive burn models for different explosives to calculate conditions for hot spot criticality.[25] Smaller colder hot spots are subcritical. They extinguish because conductive heat loss exceeds heat generation. Larger hotter hot spots are supercritical and grow until they run out of fuel.[19] A shock in a PBX that can create supercritical hot spots will produce a deflagration[26] (high speed combustion) which might evolve into a detonation if conditions permit.[4,26] A realistic depiction of PBX would have an input shock creating very many interacting hot spots.[27–29] Kapahi and Udaykumar have discussed how two nearby voids can interact to enhance or diminish the initiating shock.[15,30] Barua and co-workers[27–29] have computed the statistical distribution of hot spot temperatures and volumes in a PBX in order to identify how many of the hot spots were critical.

Although individual hot spots are difficult to study, we can probe the aggregate behavior of hot spots using nanosecond time-resolved

optical pyrometry in the visible range (442–850 nm).[31–34] Optical pyrometry measures the absolute intensity of the emission spectrum, termed the spectral radiance. When the emission is dominated by thermal emission, the spectral radiance can be fit to a graybody model to obtain time-dependent hot spot temperatures and emissivities. Emissivity is a measure of the fraction of incident light absorbed, with a black object having an emissivity of unity. The PBX used here, denoted X-PETN, is an 80:20 mixture of PETN (pentaerythritol tetranitrate) and PDMS (polydimethylsiloxane). Both of these constituents have small emissivities in the visible, but the emissivity increases greatly when the PBX is combusting.[35] Pyrometry measurements of hot spots see a lower-emissivity matrix with regions of higher emissivity that produce the thermal emission. In this case, pyrometry measures the spatially-averaged emissivity of the aggregate hot spots.[34] Knowing the emissivity of a combusting sample, it is possible to estimate the volume-averaged hot spot density in the PBX. Because we are always probing a spatial average, we cannot tell whether we are seeing one big hot spot or many tiny ones.

When an underdriven shock, a shock whose peak pressure is below the detonation pressure, traverses through a PBX, it samples regions with varying sensitivities to shock initiation.[27,29] The pressure needed to trigger the most sensitive sites is the threshold pressure, and this pressure may depend on the shock profile and duration. With above-threshold shocks, the less sensitive sites can be triggered, so the number of hot spots should increase with shock strength. In the present work, we attempt to model initiating shock propagation through an explosive charge by studying shocks in many individual tiny PBX charges, each having its own microstructure and weighing about 50 μg. Studying these individual microstructures provides insights into how a shock traversing a large explosive charge might react to different local microstructures. Here, we investigated the hot spot temperatures produced in individual charges with different microstructures and studied how the hot spot density varies with increasing shock pressure.

II. EXPERIMENTAL

A. Experimental apparatus

The experimental apparatus, which consists of a laser flyer launcher, a velocimeter, a pyrometer, a microscope, and a PBX target array, has been described in detail previously.[31,36–39] The arrangement used to shock and detect thermal emission from PBX charges is depicted in Fig. 1(a). Briefly, a pulsed Nd:YAG laser propels Al-1100 foil disks, or flyer plates, 0.5 mm in diameter and 25 μm thick, at velocities up to 4.5 km/s, in vacuum, across a 375 μm gap.[37,38,40] This vacuum, 100 mTorr, was low enough that residual gases had no effect on the flyer trajectory and compression of these gases did not produce enough light to compete with the PBX thermal emission. The flyer plates impact the surfaces of the PBX charges, which are mounted on a glass witness plate.[34] The flyer and material velocity profiles are measured with an 8 GHz photon Doppler velocimeter (PDV).[37,41,42] The 1550 nm output beam from a single-mode fiber was collimated to 600 μm diameter using an HPUCO-23A-1550-S-4.5AS collimator (Oz Optics Ltd.) and focused onto the target using a microscope objective (Nikon LU Plan Fluor 10×, 0.30 NA) with a long working distance of 17.5 mm. The focused diameter was 69 ± 3 μm. The flyer plates are solid disks due to minimal laser heating during the shock-assisted launch process,[37] and they produce planar impacts with an impact tilt less than 1 mrad.[38] A typical velocity variation at a single laser intensity was <1% and a typical time-to-impact variation was <2 ns.[38] With 25 μm Al foil flyers, the duration of the steadily-driven shock is nominally 4 ns.[37]

Coarse-grained recrystallized PETN powder was dissolved in acetone and crash-precipitated with water, which does not dissolve PETN, to produce an ultrafine powder. The powder was mixed with the PDMS binder (Sylgard 182). To aid the mixing process, the PDMS was thinned with hexanes, which do not dissolve PETN. After mixing, the hexanes were evaporated, producing a putty that was homogenized to minimize porosity, by pressing at 2000 psi for 2 min in a hydraulic press, followed by mechanically working with a Teflon-coated spatula until the putty was homogenous. The average PETN particle size was 9 μm with the majority of particles below 5 μm. Infrared spectroscopy was used to confirm that residual solvents water, hexane, and acetone were less than 1%. This laboratory-made PBX has the same composition as a commercial PBX termed XTX-8003, which has been studied previously.[43,44] The X denotes that the explosive is extrudable due to relatively high (20%) concentration of elastomeric binder. Extrudable explosives make it easier to fabricate arrays with hundreds of tiny cylindrical PBX charges. To eliminate confusion with commercial products that may have different microstructures and contain additives, we will hereafter refer to our laboratory-made PBX as X-PETN.

The X-PETN samples were fabricated in arrays containing 187 wells, each 1 mm in diameter and 42 μm thick. To fabricate the arrays, Starphire glass windows 75 × 75 × 6.35 mm^3, acting as the witness plates, were covered with a Kapton® adhesive tape 42 μm thick. A laser mill was used to cut a grid of 1.0 mm holes in the Kapton. Most of the 1 mm diameter wells in the array were packed with PBX using a Teflon-coated spatula, while a few were left empty for ranging and timing shots. The PBX charges weighed about 50 μg.

Using published Hugoniot data and detonation parameters for XTX-8003,[43] believed to be quite similar to our X-PETN, we prepared Fig. 1(b), which shows the pressures produced in X-PETN by Al flyer plates, as a function of velocity. We used the Hugoniot crossing method[45] with XTX-8003 and Al-1100 to determine the material velocity U_p of the explosive created by different Al flyer impact velocities. The XTX-8003 Hugoniot is $U_s = 1.49 + 3.30\ U_p$,[43] where U_s is the shock velocity and U_p is the material velocity. Knowing the U_p produced in the PBX allowed us to compute the pressure inside the PBX from the Hugoniot using the Rankine–Hugoniot relations.[45,46] Figure 1(b) indicates the Chapman–Jouguet pressure,[47] sometimes referred to as the detonation pressure. The detonation pressure of XTX-8003 is 17 GPa with a detonation velocity of 7.2 km/s (7.2 μm/ns).[43] The nominal boundary between underdriven and overdriven is reached with a flyer plate velocity of 2.8 km/s. Underdriven and overdriven refer to shocks in the PBX that are below or above the detonation pressure, i.e., shocks produced by flyer plate impacts at or below 2.8 km/s or above 2.8 km/s.

Figure 1(a) is a schematic depiction of what happens when a 0.5 mm diameter flyer plate impacts a 1.0 mm diameter PBX charge.

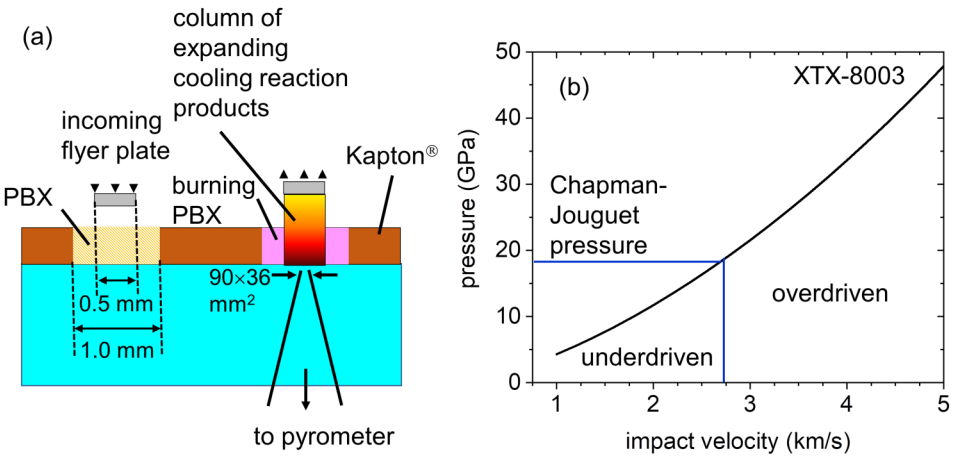

FIG. 1. (a) Schematic of the experiment (not to scale). The PBX charges were fabricated as an array of cylindrical charges 1.0 mm in diameter and 42 μm high. The 0–4.5 km/s flyer plates were launched by focusing a pulsed laser with a uniform intensity profile onto 25 μm thick Al foil. A 0.5 mm diameter cylinder of PBX is shocked. The hot gas from the shocked region expands and cools. The inner wall of the hollow cylinder, that remains for many microseconds, is ignited and it combusts releasing hot gas. (b) Pressure vs Al flyer plate velocity computed using the XTX-8003 and flyer plate Al-1100 Hugoniots.

The flyer plate creates a column of shocked PBX roughly 0.5 mm in diameter, encased by nominally unshocked PBX. A rapid reaction propagates through the shocked PBX, creating a column of super-compressed hot reaction product that blows back against the flyer plate and cools rapidly by adiabatic expansion. After the hot gas shoots out of the charge, the unshocked PBX remaining is a hollow cylinder, and the PBX on the inner cylinder wall combusts at ambient pressure for several microseconds.

B. Sample characterization

The density of X-PETN was measured by weighing the quantity needed to fill larger wells of 3 mm in diameter × 0.5 mm deep. X-PETN had a density 99 ± 3% of the theoretical maximum density (TMD) of 1.556 g/cm^3, calculated by a mass-average of PETN and PDMS densities. Scanning electron microscopy (SEM) was used to examine the PBX surface, and computed x-ray tomography (CT) using the Xradia MicroXCT-400 was performed to look at the bulk structure. The results are shown in Fig. 2. Due to the nature of our samples, we were unable to image features smaller than about 1 μm, since focusing the x-ray or electron beams more tightly than this caused the sample to decompose.[48] The SEM scans indicate there were few, if any, PETN particles larger than 10 μm. The CT scans indicate there were minimal voids large enough to see with the x-ray beams.

C. Optical pyrometry

Time-dependent temperatures and emissivities of shocked PBX were measured using our optical pyrometer.[32] It has a 10× microscope objective to collect the thermal emission and couple it to a fiber optic probe. The emission is resolved using a prism spectrograph with high throughput and minimal image distortion. Due to the way the emission is vignetted in the spectrograph, the pyrometer observes a $90 \times 36\,\mu m^2$ region at the center of the shocked region of the PBX. The spectrum dispersed by the prism is collected by 32 optical fibers that transport the different wavelengths to 32 fast photomultiplier tubes whose outputs are digitized at a rate of 1.25 GHz (800 ps). These spectra are binned and averaged to produce 15 equally-spaced points in each decade on a $\log_{10}$(time) plot.[32] It is not possible to precisely define time zero due to variations in flyer impact time and shock propagation time through the PBX of several nanoseconds. To deal with this problem, we defined the instant the observable thermal emission began to rise as 1 ns.

The pyrometer[17,18] was calibrated using a radiometric source (Ocean Optics HL-2000) coupled to a Labsphere, Inc., 2 in. diameter Spectraflect-coated uniform source, which produces spatially-uniform output calibrated to a NIST-traceable source by Labsphere. The 442–800 nm emission spectra from shocked PBX, radiometrically calibrated to yield the absolute spectral radiance, were fit to a graybody

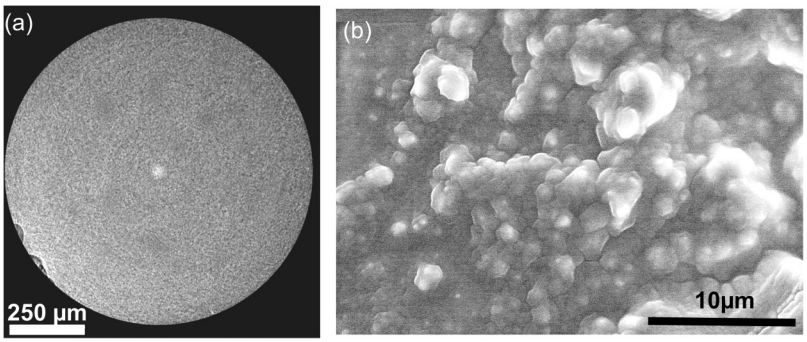

FIG. 2. Structural analysis of 1.0 mm diameter X-PETN charges. (a) X-ray CT scan of an inner plane of the 42 μm thick cylinder. (b) Scanning electron micrograph of the impact surface.

model to obtain temperature T and emissivity ε every time,[19,31]

$$L(T,\lambda)d\lambda = \varepsilon \cdot \frac{2hc^2 d\lambda}{\lambda^5\left[e^{\frac{hc}{\lambda kT\lambda}} - 1\right]}, \quad (1)$$

where $L(T,\lambda)d\lambda$ is the spectral radiance for a graybody with emissivity ε. The spectral maximum is given by Wien's displacement law,[49]

$$\lambda_{\max}\ (\mu\text{m}) = \frac{2900}{T}. \quad (2)$$

For instance, the spectral maximum for a 2500 K blackbody or graybody is located at 1.16 μm. Because our spectral range of observation is 442–800 nm, for temperatures in the 1500–3600 K range, the spectral maximum in the near-infrared is not seen with our pyrometer.

Equation (1) describes a hot body with a spatially-uniform emissivity and needs to be modified to account for hot spots.[33] The X-PETN consists of colorless materials, so the emissivity is low in the visible. As discussed previously, Eq. (1) describes a hot body with a spatially-uniform emissivity and needs to be modified to account for hot spots.[33] The higher-emissivity hot spots are distributed in space within the lower-emissivity unreacted PBX. As discussed previously,[34] we modified Eq. (1) to describe a lower-emissivity matrix with higher-emissivity regions. We assume that there is one intrinsic emissivity ε for the hot spot regions that does not vary with time or hot spot density. In that case, we can define the parameter Φ,[33]

$$\Phi = \varepsilon \times V^*, \quad (3)$$

where Φ is the "spatially-averaged emissivity" measured by our spectrometer, ε is the intrinsic emissivity of the hot material, and V^* is the volume fraction of hot spot emitters. The hot spot emissivity is difficult to measure, but we can estimate it based on the intrinsic emissivity, which is the emissivity seen when all the PBX in view is burning. With this estimated intrinsic emissivity, we can estimate V^*, the volume fraction of hot spot emitters.

The spectral radiance was obtained by averaging typically 25 shots at each flyer speed. Before averaging, we examined each transient and discarded obvious outliers. There were never more than 1–2 outliers in any batch of 25, and the outliers appear to be due to overfilled sample wells or charges which picked up debris from the explosion of a neighboring charge. The error bars for emissivity were significantly larger than for temperature. The emissivity depends on the overall intensity of the spectral radiance, and this intensity is sensitive to temperature variations. The intensity, when integrated over all wavelengths, varies as T^4.[49] Over the finite wavelength range we use, 442–850 nm, in the 3000 K range, the wavelength-integrated amplitude varies somewhat more strongly with T. Therefore, the small temperature variations produced larger emissivity variations.

III. RESULTS

A. Emission spectra of shocked PBX

The emission spectra of shocked X-PETN generally fit well to a graybody distribution. However, comparing the spectral radiance to theoretical graybody spectra indicate that there are some deviations which are most prominent at shorter times and lower impact velocities, but negligible at longer times and at higher impact velocities. Figure 3 compares the spectral radiance to theoretical graybody spectra in selected cases when the nonthermal contributions were the greatest. The nonthermal contributions to the spectral radiance appear as a positive deviation near 650 nm. Such positive deviations are ordinarily associated with poorly-resolved atomic or small-molecule emission in less-dense regions of the exploding sample. However, the deviations were small enough that they did not affect the temperature accuracy.

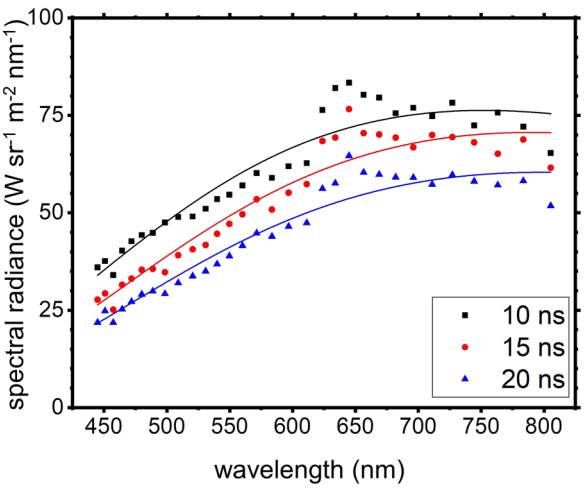

FIG. 3. Spectral radiance at shorter times for X-PETN with a 2.8 km/s impact. There is a nonthermal component around 650 nm, which is greatest at shorter times and lower impact velocities. The smooth curves were fits to the graybody model [Eq. (1)]. At higher impact velocities and longer times, the nonthermal part becomes inconsequential.

B. Temperature profiles for shocked PBX

Time-dependent temperature profiles for shocked X-PETN are shown in Fig. 4 for impact velocities from 2.0 to 4.5 km/s. A weak emission was observed with 1.5 km/s impacts, but below 2.0 km/s, the emission was too weak and noisy to determine reliable temperature and emissivity profiles. The error bars in Fig. 4 represent the 95% confidence limits for fitting the data to the graybody model. In order to avoid cluttering the figures with error bars, we just displayed the error bars for the 2.0 km/s impacts, which were similar at other impact velocities.

In all the temperature profiles, there was an initial period of a few nanoseconds where the temperature was constant, and, surprisingly, this initial hot spot temperature was independent of impact velocity. It is surprising because the faster flyer plates have five times the total kinetic energy of the slower ones and would be expected to deposit much more energy and create more larger and hotter hot spots. Following the brief period of constant temperature, there is a period of cooling lasting several hundred nanoseconds. The cooling becomes much more dramatic for overdriven

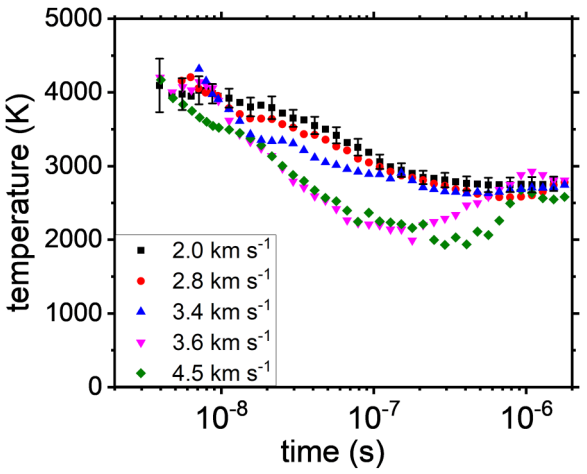

FIG. 4. Time-dependent temperature profiles from X-PETN impacted at the indicated velocities. Error bars were omitted from all but the slowest velocity for clarity. Typical relative error in the temperature determination is 5% until 10^{-8} s and 3% thereafter.

shocks. The cooling rates can be enormous. The slower cooling produced by underdriven shocks was 1000 K in 300 ns ($dT/dt \approx 3 \times 10^9$ K/s), and the faster cooling produced by overdriven shocks is 2000 K in 100 ns ($dT/dt \approx 2 \times 10^{10}$ K/s). After this rapid cooling, at longer times around 1 μs, all the temperature profiles converge to the same temperature, 2700 K, regardless of impact velocity. This 2700 K longer-time temperature is the temperature associated with hot gases evolved from the combustion of the part of the PBX charge that was not shocked [see Fig. 1(a)].

The results in Fig. 4 were obtained by averaging the spectral radiances from about 25 different PBX charges. However, we can also measure the spectral radiance and temperature profile of shocked individual charges. We focus on the initial hot spot temperature, the nearly constant temperature in the 5–10 ns range. In Fig. 5, we plotted histograms of the initial hot spot temperatures

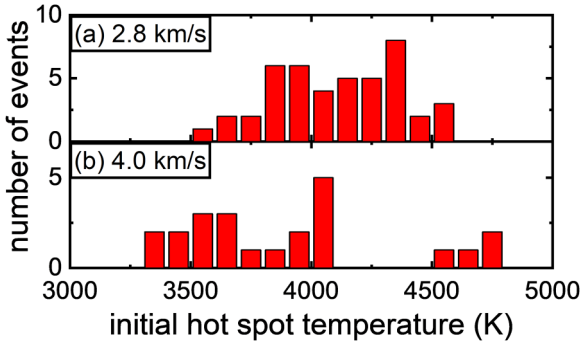

FIG. 5. Initial hot spot temperatures for individual charges of X-PETN with underdriven (2.8 km/s impact) or overdriven (4.5 km/s impact) shocks.

with 2.8 (underdriven) and 4.0 km/s (overdriven) impacts. These results are representative for the underdriven and overdriven cases. The average temperature of these histograms is about 4000 K, but as seen in Fig. 4, the distribution changes with impact velocity. With underdriven shocks, the initial hot spot temperatures clustered around 4000 K, but with overdriven shocks, the distribution became broader, with more extreme higher and lower temperatures.

C. Emissivity profiles for shocked PBX

In Fig. 6, we show the spatially-averaged emissivities Φ and the corresponding temperature profiles from shocked X-PETN at shorter times. The emissivity measurements can be used to track hot spot growth and decay. We can crudely estimate the hot spot volume fraction V^*. In prior experiments on combustion of polymer-bonded RDX (1,3,5-Trinitroperhydro-1,3,5-triazine), the emissivity of RDX at high temperature was found to be on the order of 0.5,[35] which ought to be a reasonable estimate for X-PETN. Figure 6(b) shows the emissivity at shorter times reaches a value of about 0.02 with lower impact velocity and 0.1 with higher impact velocity. Using $\varepsilon = 0.5$ in Eq. (2) shows that during the hot spot generation period, the initial hot spot volume fraction is of the order of 4% with an underdriven shock and 20% with an overdriven shock.

The X-PETN spatially-averaged emissivities in Fig. 6(b) show an initial growth phase and then a brief level phase followed by a second growth phase. The initial growth phase takes 11 ns. The level phases last about 20 ns.

D. Shock strength-dependent growth in reaction volume

The spatially-averaged emissivities Φ increased with increasing impact velocity. Even though the average hot spot temperatures did not increase with impact velocity, the hot spot volume fractions V^* did. In Fig. 7, we plotted Φ near the radiance peak, which was at about 11 ns, but the precise choice of this time made little difference. The model curve is discussed below.

IV. DISCUSSION

A. Hot spot temperature dynamics

The X-PETN temperature profiles in Fig. 4 may be described as having three parts. First is a hot spot generation period lasting about 10 ns, where the average temperature of 25 or more samples is always ~4000 K, regardless of impact velocity. Subsequently, there were two distinct types of cooling processes, a slower cooling with underdriven shocks and a faster cooling with overdriven shocks. After the cooling process, all the temperature profiles converged around 1 μs to the same temperature of about 2700 K.

The initial hot spot temperatures of ~4000 K in Fig. 4, remarkably, do not increase with impact velocity. However, the hot spot volume fraction, as expressed by the increased spatially-averaged hot spot emissivity Φ shown in Fig. 7, increases a great deal with impact velocity.

The 50–100 ns rapid cooling can be explained with reference to Fig. 1(a), as resulting from the fast adiabatic expansion of the gas produced by PBX decomposition. The sudden increase in the cooling rate between the underdriven and overdriven regimes

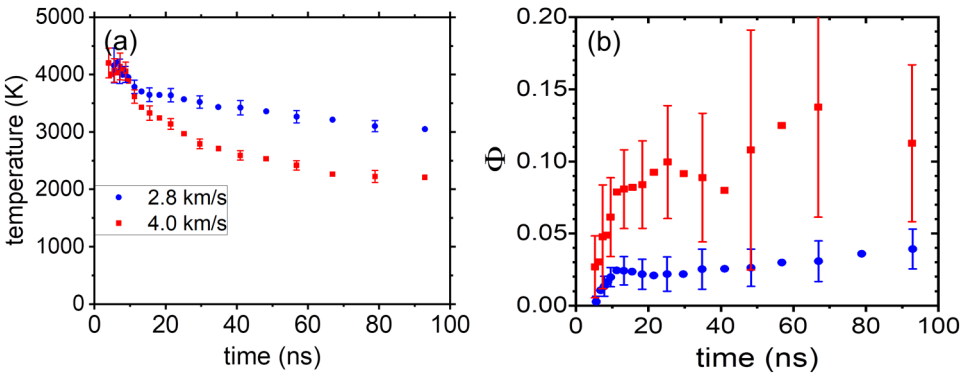

FIG. 6. (a) Temperature profiles for X-PETN with 2.8 km/s and 4.0 km/s impacts. (b) Corresponding spatially-averaged radiance (Φ) profiles, where Φ is proportional to the hot spot volume fraction.

indicates that the detonation velocity is in the region where gas production first becomes significantly more efficient. Additionally, there may be a supporting role for thermal conduction during the cooling period. We can make a crude evaluation of the thermal conduction from hot spot to unreacted solid by estimating the thermal diffusivity of PETN to be $D = 10^{-3}$ cm^2/s, typical for these type of materials.[50] Using the relationship $d = (2Dt)^{1/2}$, where d is a measure of the distance heat diffuses in time t, we find that for $t =$ 100 ns, $d = 140$ nm. So thermal conduction from hot spots to colder solid or fluid media could assist the fast cooling for hot spot regions 100 nm or smaller.

The temperature convergence at longer times is a result of the experimental geometry depicted in Fig. 1(a). After the shocked material explodes, the rest of the X-PETN charge is in the form of a hollow cylinder nominally 0.5 mm inner diameter and 1.0 mm outer diameter, but the inner wall was ignited by the hot reaction products blowing out of the charge [Fig. 1(a)]. The combustion temperature of this inner wall material should not depend on precisely what happened in the shock region that caused it to ignite, so regardless of impact velocity, all the temperature profiles at longer times converge to the same temperature.

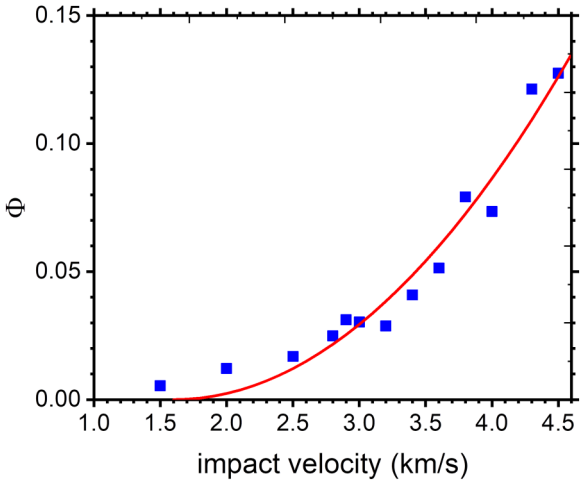

FIG. 7. Impact velocity dependence of spatially-averaged emissivity Φ at $t = 11$ ns for X-PETN. Solid curves are a model that assumes a distribution of barrier energies to hot spot creation having a threshold and a constant distribution above threshold.

B. Hot spot growth at shorter times

The hot spots were generated within about 11 ns of impact in X-PETN, based on the initial rise of emissivity in Fig. 6(b). For our 40 μm thick PBX charges, a shock at the detonation velocity (7.2 μm/ns) runs through the charge in about 6 ns. The shock duration is nominally 4 ns, so although any volume element of the PBX sees the initiating shock for just 4 ns, hot spots are generated over a 10 ns period. Thus, shock generation of hot spots in X-PETN appears to occur instantaneously (i.e., within our time resolution of a few nanoseconds) behind the shock front.

According to the emissivity results in Fig. 6(b), after the hot spot generation period, there is a second growth phase which represents the explosive growth of supercritical hot spots[19] into deflagration. But in between hot spot generation and deflagration, there is an intermediate phase with interesting behavior. The hot spot volume fraction, as judged by the emissivity, stays constant for a few tens of nanoseconds. We do not interpret the constant emissivity in the time between hot spot generation and explosive growth as arising from static hot spots, but rather a competition between extinguishing the subcritical hot spots and growth of supercritical hot spots. After enough subcritical hot spots have extinguished, the overall emissivity can grow.

The initial hot spot temperatures, with an average of 4000 K and some reaching 4700 K (Fig. 5), are significantly greater than what could be expected for ambient X-PETN combustion, which according to the longer-time limit in Fig. 4 would be about 2700 K. The high pressures and densities during the shock would not increase the PETN combustion temperature, because high pressure slows down the rates of this type of reaction, where larger molecules decompose into many smaller ones.[51,52]

Since PETN combustion cannot explain the high temperatures we see, we have to look at other mechanisms such as reactive energy focusing in the microstructure and adiabatic compression of gas pockets, most smaller than 1 μm.

A number of theoretical works on shock collapse of voids of various sizes and shapes in nonreactive or reactive materials have

shown that mechanical energy can be focused during the collapse to produce hot regions and hot chemistry. The hottest regions are produced by voids with more surface area.[25,53] Shan and co-workers[24] used both atomistic and continuum hydrodynamics simulations to study collapse of a cylindrical void in PETN. They showed that void collapse produced a triangular hot zone from a jet of hot molecules. Wood and co-workers[26] showed that even with voids as small as 40 nm, highly nonequilibrium and highly energetic chemical reactions can occur on the picosecond time scale.

Shocking a gas produces much higher temperatures than shocking a solid. Our group previously studied the initial hot spot temperatures after saturating the voids in X-PETN with various gases.[34] We proved the high initial hot spot temperatures were, at least in part, produced by gases in the void, since higher heat capacity gases such as butane produced much lower temperatures.[34] Even when the X-PETN was in 100 mTorr vacuum, initial hot spot temperatures above 3500 K were observed, which were attributed to compression of gases generated by the volatile explosive during the early stage of void collapse.[34]

This discussion suggests that the high initial hot spot temperatures we observe are produced by a combination of gas compression and reactive mechanical focusing that occurs during shock collapse of even quite small voids. It should be kept in mind that when observing a material with a distribution of temperatures, pyrometry is most sensitive to the hottest parts, since the rate of thermal emission increases as a high power of temperature. Thus, our focus on the high initial hot spot temperatures does not preclude the coexistence of the high-temperature hot spots we see with pyrometry and other types of hot spots reacting at temperatures closer to the combustion temperature.

C. Model for hot spot generation

We have developed a simple model, depicted in Fig. 8, to understand how the initial hot spot temperatures could be nearly independent of impact velocity while the hot spot concentration could increase with impact velocity. In this model, the shock provides the energy needed to get over an ignition barrier to trigger hot spot generation. This barrier height is much smaller than the heat of combustion, so the amount of energy liberated by the explosive is far greater than what was input by the shock. In that case, it would be the explosive energy release that determines the temperature, rather than the energy of the incoming shock.

According to our results, there must be a distribution of both heats of combustion and barrier heights in each microstructure. These distributions are indicated in the schematic diagram in Fig. 8. Information about the distributions of heats of combustion, as depicted schematically in Fig. 8(b), is obtained from Fig. 5, where we plotted the initial hot spot temperatures of individual charges. Each charge has a unique microstructure, and each microstructure produces a different quantity of heat. It could be as simple as random fluctuations in the relative proportions of explosive and binder.

The distribution of barrier heights is needed to explain the emissivity growth in Fig. 7, which reflects the increase in hot spot volume fraction, with increasing impact velocity. Since no hot spot emission was observed for impacts below about 1.5 km/s, then the first signs of hot spot emission represent triggering of sites with the lowest barriers to shock initiation. In other words, 1.5 km/s impacts are just sufficient to trigger sites with the threshold barrier height.

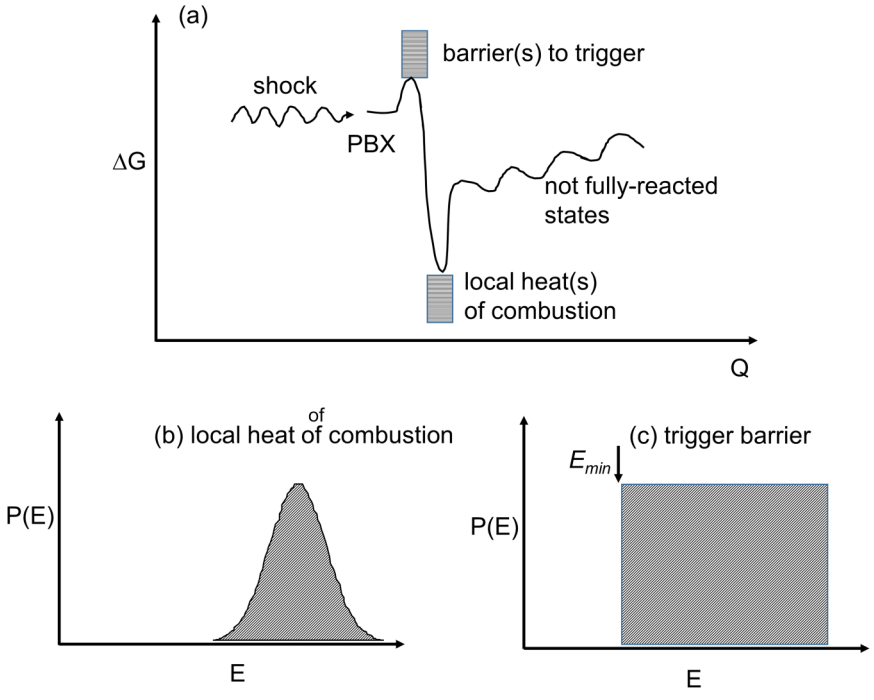

FIG. 8. (a) Model for shock generation of hot spots that would produce a temperature largely independent of shock strength, while the hot spot concentration would increase quadratically with impact velocity. (b) Proposed distribution of heats of combustion which determines the initial hot spot temperature of small charges. (c) Proposed distribution of barrier heights, which is consistent with impact velocity dependence of hot spot volume fraction.

The emissivity growth implies that there are many more sites with above-threshold barriers. We cannot directly determine the distribution of hot spot trigger barriers, but we can compute the hot spot volume fraction for any assumed barrier height distribution. The simplest such distribution would be a distribution of barrier heights above the threshold value that is nominally independent of the barrier height, as depicted in Fig. 8(c).

The material velocity U_p in the explosive is approximately proportional to the impact velocity. According to the Rankine–Hugoniot equations, the energy in the shock is quadratic in the material velocity U_p.[45] Thus, a flat distribution of barrier heights, as in Fig. 8(c), implies a quadratic increase with flyer velocity, of the number of barriers that can be accessed. Figure 7 shows that such a quadratic dependence provides a good fit to the data. Based on this analysis, we can say that there must be a minimum barrier height to trigger hot spot formation, and the distribution of barrier heights is roughly constant above this threshold.

V. SUMMARY AND CONCLUSIONS

Shock-induced hot spot formation in a model PBX, X-PETN, was studied by high dynamic range optical pyrometry. Each of the individual PBX charges had a somewhat different initial hot spot temperature, but the average over 25 or more shots was about 4000 K and, surprisingly, it was independent of impact velocity for velocities above the ~1.5 km/s threshold velocity needed to see hot spots by pyrometry. The density of hot spots, as monitored by the change in emissivity with shock, increased rapidly with impact velocity above 1.5 km/s. The distribution of initial hot spot temperatures and the increase in hot spot density with shock strength suggested a simple model where the initial hot spot temperature depended on the microstructure of each explosive charge, and the number of barriers to trigger hot spot formation was, above a threshold value, a roughly constant function of energy.

These observations can be combined to create a picture of how shocks produce hot spots in PBX. Underdriven shocks produce hot spots clustered around 4000 K, most likely by compression of gas and reactive energy focusing in micro- and nanopores. An overdriven shock produces many more hot spots since it is capable of triggering many more sites. These hot spots also have a temperature distribution with a mean of 4000 K, but this distribution includes many colder and a few hotter hot spots. The colder hot spots are the ones in regions of rapid expansive cooling. The hotter spots are the ones where gas compression and reactive energy focusing create temperatures much greater than normal combustion.

ACKNOWLEDGMENTS

The research described in this study is based on work at the University of Illinois, supported by the U.S. Army Research Office under Award No. W911NF-19-1-0037 and the U.S. Air Force Office of Scientific Research under Award No. FA9550-16-1-0042. This work was performed under the auspices of the U.S. Department of Energy by Lawrence Livermore National Laboratory under Contract No. DE-AC52-07NA27344 and was supported by the LLNL-LDRD Program under Project No. 18-SI-004. SEM images were collected in the Materials Research Laboratory Central Research Facilities at UIUC. CT data were taken at the Microscopy Suite at the Beckman Institute for Advanced Science and Technology at UIUC. Belinda P. Johnson acknowledges support from the National Science Foundation Graduate Research Fellowship Program under Grant No. DGE-1144245 and the Alfred P. Sloan Foundation's Minority Ph.D. (MPHD) Program, awarded in 2016. Lawrence Salvati III acknowledges support from a PPG-MRL graduate research award.

REFERENCES

[1]J. E. Field, Acc. Chem. Res. **25**, 489 (1992).
[2]M. R. Baer, Thermochim. Acta **384**, 351 (2002).
[3]W. L. Perry, B. Clements, X. Ma, and J. T. Mang, Combust. Flame **190**, 171 (2018).
[4]J. Zhang and T. L. Jackson, Shock Waves **29**, 327 (2019).
[5]T. Urbanski, *Chemistry and Technology of Explosives* (Pergamon Press, Oxford, 1984).
[6]E. J. Welle, C. D. Molek, R. R. Wixom, and P. Samuels, J. Phys. Confer. Ser. **500**, 052049 (2014).
[7]E. J. Welle, C. D. Molek, R. R. Wixom, P. Samuels, and J. T. Langhals, J. Phys.: Conf. Ser. **500** (2014).
[8]R. Knepper, A. S. Tappan, R. R. Wixom, and M. A. Rodriguez, J. Mater. Res. **26**, 1605 (2011).
[9]Q. An, W. A. Goddard, S. V. Zybin, A. Jaramillo-Botero, and T. T. Zhou, J. Phys. Chem. C **117**, 26551 (2013).
[10]M. R. Manaa and L. E. Fried, in *Advances in Quantum Chemistry*, edited by J. R. Sabin (Elsevier Academic Press, Inc., San Diego, 2014), Vol. 69, p. 221.
[11]L. E. Fried and C. Tarver, AIP Conf. Proc. **370**, 179 (1996).
[12]T. R. Shan, R. R. Wixom, and A. P. Thompson, Phys. Rev. B **94**, 054308 (2016).
[13]B. A. Khasainov, B. S. Ermolaev, H.-N. Presles, and P. Vidal, Shock Waves **7**, 89 (1997).
[14]A. Mandal and K. A. Gonthier, Shock Waves **25**, 589 (2015).
[15]A. Kapahi and H. S. Udaykumar, Shock Waves **23**, 537 (2013).
[16]A. L. Brundage, R. R. Wixom, A. S. Tappan, and G. T. Long, AIP Conf. Proc. **1195**, 315 (2009).
[17]J. Gilbert, S. Chakravarthy, and K. A. Gonthier, J. Appl. Phys. **113**, 194901 (2013).
[18]J. W. Mintmire, D. H. Robertson, and C. T. White, Phys. Rev. B **49**, 14859 (1994).
[19]C. M. Tarver, S. K. Chidester, and A. L. Nichols III, J. Phys. Chem. **100**, 5794 (1996).
[20]T. T. Zhou, L. C. Liu, W. A. Goddard, S. V. Zybin, and F. L. Huang, Phys. Chem. Chem. Phys. **16**, 23779 (2014).
[21]T. T. Zhou, J. F. Lou, Y. G. Zhang, H. J. Song, and F. L. Huang, Phys. Chem. Chem. Phys. **18**, 17627 (2016).
[22]K. Nomura, R. K. Kalia, A. Nakano, and P. Vashishta, Appl. Phys. Lett. **91**, 183109 (2007).
[23]T.-R. Shan, R. R. Wixom, A. E. Mattsson, and A. P. Thompson, J. Phys. Chem. B **117**, 928 (2013).
[24]T.-R. Shan, R. R. Wixom, and A. P. Thompson, Phys. Rev. B **94**, 054308 (2016).
[25]N. K. Rai and H. S. Udaykumar, Phys. Fluid. **31**, 016103 (2019).
[26]M. A. Wood, M. J. Cherukara, E. M. Kober, and A. Strachan, J. Phys. Chem. C **119**, 22008 (2015).
[27]A. Barua, Y. Horie, and M. Zhou, J. Appl. Phys. **111**, 054902 (2012).
[28]A. Barua, S. Kim, Y. Horie, and M. Zhou, J. Appl. Phys. **113**, 064906 (2013).
[29]A. Barua, S. Kim, Y. Horie, and M. Zhou, J. Appl. Phys. **113**, 184907 (2013).
[30]A. Kapahi and H. S. Udaykumar, Shock Waves **25**, 177 (2015).
[31]W. P. Bassett and D. D. Dlott, J. Appl. Phys. **119**, 225103 (2016).
[32]W. P. Bassett and D. D. Dlott, Rev. Sci. Instrum. **87**, 103107 (2016).
[33]W. P. Bassett and D. D. Dlott, Appl. Phys. Lett. **109**, 091903 (2016).
[34]W. P. Bassett, B. P. Johnson, N. K. Neelakantan, K. S. Suslick, and D. D. Dlott, Appl. Phys. Lett. **111**, 061902 (2017).
[35]M.-W. Chen, S. You, K. S. Suslick, and D. D. Dlott, Rev. Sci. Instrum. **85**, 023705 (2014).
[36]D. D. Dlott, AIP Conf. Proc. **1793**, 020001 (2017).

[37]A. D. Curtis, A. A. Banishev, W. L. Shaw, and D. D. Dlott, Rev. Sci. Instrum. **85**, 043908 (2014).
[38]A. A. Banishev, W. L. Shaw, W. P. Bassett, and D. D. Dlott, J. Dyn. Behav. Mater. **2**, 194 (2016).
[39]M. Bhowmick, E. J. Nissen, and D. D. Dlott, J. Appl. Phys. **124**, 075901 (2018).
[40]K. E. Brown, W. L. Shaw, X. Zheng, and D. D. Dlott, Rev. Sci. Instrum. **83**, 103901 (2012).
[41]J. Weng, X. X. Wang, Y. Ma, H. Tan, L. Cai, J. Li, and C. Liu, Rev. Sci. Instrum. **79**, 113101 (2008).
[42]M. Bhowmick, W. P. Basset, S. Matveev, L. Salvati III, and D. D. Dlott, AIP Adv. **8**, 125123 (2018).
[43]D. Stirpe, J. O. Johnson, and J. Wackerle, J. Appl. Phys. **41**, 3884 (1970).
[44]C. A. Campos, "The effects of diameter and temperature on XTX-8004 detonation velocity," USDOE Report No. MHSMP-80-50, October 1980.
[45]J. W. Forbes, *Shock Wave Compression of Condensed Matter. A Primer* (Springer, New York, 2012).
[46]S. P. Marsh, *LASL Shock Hugoniot Data* (University of California Press, Berkeley, CA, 1980).
[47]W. Fickett and W. C. Davis, *Detonation* (University of California Press, Berkeley, CA, 1979).
[48]W. P. Bassett and D. D. Dlott, AIP Conf. Proc. **1793**, 060012 (2017).
[49]R. S. Berry, S. A. Rice, and J. Ross, *Physical Chemistry*, 2nd ed. (Oxford, New York, 2000).
[50]J. F. Baytos, "Specific heat and thermal conductivity of explosives, mixtures and plastic-bonded explosives determined experimentally," Los Alamos Scientific Laboratory Report LA-8034-MS, September 1979.
[51]G. J. Piermarini, S. Block, and P. J. Miller, J. Phys. Chem. **91**, 3872 (1987).
[52]G. J. Piermarini, S. Block, and P. J. Miller, *Effects of Pressure on the Thermal-Decomposition Rates, Chemical-Reactivity and Phase-Behavior of HMX, RDX and Nitromethane* (Kluwer Academic Publishers, Dordrecht, 1990), Vol. 309.
[53]N. K. Rai and H. S. Udaykumar, Phys. Rev. Fluids **3**, 033201 (2018).